A Power and Performance Study of Compact *L*-Band Total Power Radiometers for UAV Remote Sensing Based in the Processing on ZYNQ and ARM Architectures

Daniel Ernesto Mera , *Member, IEEE*, Rafael A. Rodríguez Solís , *Senior Member, IEEE*, Lorenzo Reyes*, Member, IEEE*, Roy Armstrong, William J. Hernandez, and Alba L. Guzmán-Morales

Abstract—This article presents a study on the power consumption and performance analysis of a small, portable, and ultra-low power total power *L*-band radiometer. The article explores two processing architectures: the ZYNQ 7010 and the ARM A8 embedded microprocessor. The processing algorithm based in C++ was tested for different clock frequencies, ADC sampling speeds, and sizes of the ADC buffer. To reduce the power consumption and the algorithm execution time, high-level and system-level optimizations, along with fixed-point $Q(16,16)$ data representation, were applied to the main code running on LINUX Debian V8. In the case with the ZYNQ 7010, the optimizations had no notable impact on reducing power or execution time in comparison with the ARM A8, where significant variations were measured, showing a tradeoff between power consumption and algorithm performance that limits the processing capability and the system flight time. The ZYNQ 7010 runs the algorithm faster, but the power consumption is higher than the ARM A8. Using the fixed-point $Q(16,16)$ implementation reduced the power consumption and the execution time in both architectures. Based on these results, we developed a heuristic methodology to minimize power consumption and increase the performance. Energy consumption savings for the radiometer during 20 min of flight was **48%**. The size of the radiometer was reduced to 30 cm × 30 cm × 10 cm, with a weight of 1.36 kg, (3 lb) allowing the system be carried by small drones. The results were validated measuring salinity at two locations in Western Puerto Rico.

Index Terms—C programming, compact radiometer, embedded system, LINUX, low power, microwave radiometry, performance, salinity remote sensing.

I. INTRODUCTION

MICROWAVE radiometers have different applications in agriculture, drought monitoring, in water resource management, and assessing vegetation health [1]. The satellite radiometric data applied to weather forecasting helps to improves the prediction models of hurricanes and climate changes such as "La Niña Phenomenon."

The main limitations of ground-based radiometers are mobility and portability, due to their size, weight in the tens of kilograms, and high power consumption (>200 W), like the radiometers built in [1] and [2]. This limitation affects data acquisition in the field, the scope of the field of view, the resolution, and the quality of the data [2].

Few works in the design of radiometers have focused on reducing the size, weight, and power consumption of microwave radiometer systems, [3], [4]. Dai *et al*. [3] present a radiometer for soil moisture applications at *L*-band (1.4 GHz) for validation and calibration of the SMAP (soil moisture active passive) satellite sensor. The radiofrequency receiver measures 30 cm, weights 3 lb, the power consumption is >12 W, and the processing and storage modules are separated. The processing system is a raw datalogger, and the information is processed on ground after the flight. The *L*-band radiometer in [4] also uses raw dataloggers for future processing, and the power consumption is approximately 10 W, limiting the flight time. Another example is the miniaturized multiband radiometer for cubesats for the MiRaTA project [5] being developed by MIT and MIT Lincoln Laboratories. The system will retrieve data in three bands: *V*-band (50–57 GHz); *G*-band (175–191 GHz); and *G*-band (205 GHz), and will be used to develop accurate weather forecasting models.

Several studies show that the back-end processing system is one of the largest contributors in the power consumption of a radiometer mounted on unmanned aerial vehicles (UAVs) [6]–[9]. Most of these works used microprocessors and FPGAs to process the radiometric data, or data-loggers to store the raw data in flight and process the data on ground after the flight. For example, Asif *et al*. [7] use an FPGA to process the radiometric data and the power consumption was higher than 8 W. These works do not take into consideration how the power consumption of the back-end processing system impacts the performance, flight time, battery capacity, weight, and size of the radiometer.

Daniel Ernesto Mera, Rafael A. Rodríguez Solís, Lorenzo Reyes, and William J. Hernandez are with Electrical and Computer Engineering Department, Mayagüez, PR 00680 USA (e-mail: daniel.mera@upr.edu; rafael.rodriguez19@upr.edu; lorenzo.reyes@upr.edu; william.hernandez@upr.edu).

Roy Armstrong and Alba L. Guzmán-Morales are with Marine Sciences Department, University of Puerto Rico at Mayagüez, Mayagüez, PR 00680 USA (e-mail: roy.armstrong@upr.edu; alba.guzman2@upr.edu).

This article presents an approach to design a small size, low weight, and low power (SWaP) digital receiver for a compact *L*-band total-power radiometer, and analyzes the tradeoffs between power consumption and performance of the processing system.

This article analyzes two processing system architectures: an ARM A8 microprocessor, and the ZYNQ 7010 hybrid hardware (ARM A9 microprocessor + Xilinx 7-series FPGA). Based on the experimental results, a heuristic methodology is proposed to process the radiometric data efficiently in terms of power consumption and performance. This heuristic methodology allowed us to design the low SWaP digital receiver for the small UAV mounted compact *L*-band radiometer with faster data processing and significant reduction in overall power consumption. The main contributions of this article are the heuristic methodology, based on low power optimizations at high-level and operating system-level; a low power usage mode; a power efficient scanning method, using the height and speed of the UAV; and the inclusion of fixed-point math in the calculations and data formatting. The results obtained for the proposed methodology resulted in a power consumption of less than 2.3 W and an algorithm execution time of 19 ms for the ZYNQ 7010, and a power consumption of less than 1.5 W and 65 ms execution time for the ARM A8, at a clock speed of 1 GHz. These results represent a 48% savings in radiometer energy consumption in a 20-min flight.

The rest of this article is organized as follows. Section II discusses our previous work. Section III presents the system description, Section IV explains the front-end characterization. Section V shows the processing algorithm and optimizations, Section VI presents the results and analysis. Section VII discusses the proposed heuristic methodology. Section VIII presents the validation results of the built UAV compact radiometer. Finally, Section IX concludes this article.

II. PREVIOUS WORK

A. L-Band Radiometer

We presented the design and construction of the first prototype of a small, lightweight low power *L*-band total power radiometer in [9]. In [6], an analysis of the impact of applying high-level optimizations to the processing program on the power consumption and processing speed was performed. The processing program was written in C++, and ran on Debian Linux V.8 on an ARM A8 embedded microprocessor (Beaglebone Black). In [10], we performed a statistical analysis of the effect of the optimizations using design of experiments techniques to better understand their impact in the power consumption and the execution time.

This article includes new results of power and performance of the radiometer using the ZYNQ 7010 architecture and the methodology to optimize the power consumption and the algorithm execution time. Additionally, it shows a power efficient scanning method and the results of field measurements in Western Puerto Rico. Table I gives the characteristics of the main components of the new radiometer version.

III. SYSTEMS DESCRIPTION

Two implementations of the radiometer were designed and built; both use the same front end, antenna, detector, and

TABLE I
L-BAND RADIOMETER SPECIFICATIONS

| Parameter	Description
Frequency	1.419 *GHz*
Antenna	2x2 Array of microstrip patches; G_A = 12.5 dB; B = 22 MHZ; η_b= 97.34%, Beamwidth = 52 deg; Dimensions: 21 cm x 21 cm; Substrate: Rogers RT Duroid 5870, ε_r=2.33; Footprint: 63.8 m diameter at 60 m height.
Receiver	Total Gain = 92 dB; *NFsys* = 0.6 dB, $\Delta G/G$ = 0.002; T'_{REC} = 232.34 K.
Resolution	ΔT = 1.70 K at τ = 7 ms.
Sensor board	GPS receiver, (GY-BME280), and the MPU 6050.
Back End Processor	ARM A8 – ADC sampling: 1 MS/s; Clock Frequency: 1 GHz - 300 MHz; 4 Gb SD card. ZYNQ 7010 – ADC sampling: 1 MS/s; Clock Frequency: 1 GHz - 300 MHz; 4 Gb SD card.
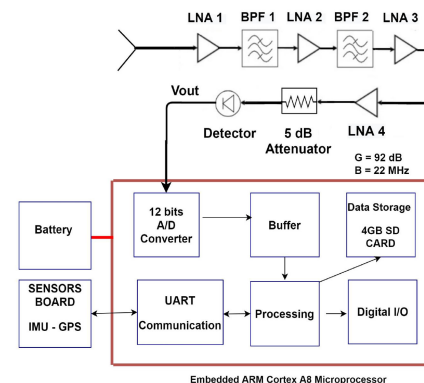
Fig. 1. *L*-band radiometer based on ARM A8 architecture.

sensors board. The difference is in the processing system and the implementation of the algorithm. Fig. 1 shows the block diagram of the *L*-band total power radiometer system with the ARM A8 microprocessor (Beaglebone Black). Fig. 2 shows the radiometer with the ZYNQ 7010 (zybo z7 board) architecture. The ZYNQ 7010 is a new hybrid architecture (ARM A9 microprocessor and a Xilinx 7-series FPGA) with AXI (Advanced eXtensible Interface) communication channels.

A. Processing System With the ARM A8 Microprocessor (Beaglebone Black)

The data acquisition, buffering, filtering, storage, and processing is done by an ARM A8 microprocessor running at a maximum clock frequency of 1 GHz [11]. The processing algorithm, written in C++, runs on embedded Debian Linux V.8. The internal ADC has 7 channels at 12 bits, with a maximum
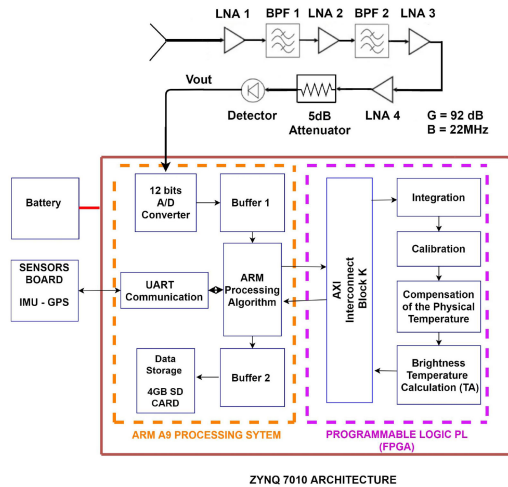
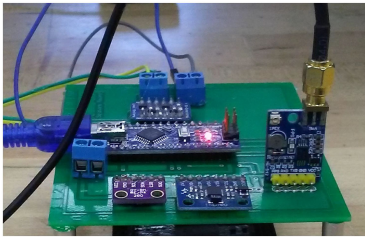Fig. 2.   *L*-band radiometer based on ZYNQ architecture.

Fig. 3.   Sensors board with GPS, altimeter, and accelerometer.

sampling rate of 1 MS/s. The data at the output of the detector are buffered into a dynamic array later filtered digitally. The system has a sensor board, shown in Fig. 3, that includes an Arduino Atmega328 microcontroller, a GPS receiver, a high precision atmospheric pressure sensor module (GY-BME280), the MPU 6050 (6-axis IMU sensor) and temperature sensor. After processing, the data is stored in an expandable 4 GB SD-card.

B. Processing System With the ZYNQ Architecture

The hybrid ZYNQ 7010 architecture (FPGA + ARM A9 microprocessor) from Xilinx has low power consumption ($<$ 3.5 W), high sampling speed at 1 MS/s and high processing capability. It can be synthetized for high production with VLSI, and the algorithms can be easily parallelized with the Vivado tools [12]. Fig. 2 shows the hardware implementation using the ZYNQ 7010 architecture, the design problem was addressed distributing the workload as follows: the calculation portions; including floating-point operations, were assigned to the FPGA side and the control, data acquisition, and sensors data retrieval were done with the microprocessor side (ARM A9). This configuration was, according to the experiments, the most efficient in terms of power and execution time as shown in Section VI. This is because the computationally intensive operations result in a bottleneck that is well mitigated with the hardware acceleration in the FPGA since it can be fully tailored and optimized for a particular task [12]. The power consumption was less than 2.4 W, and the execution time of the system was reduced to 19 ms at a
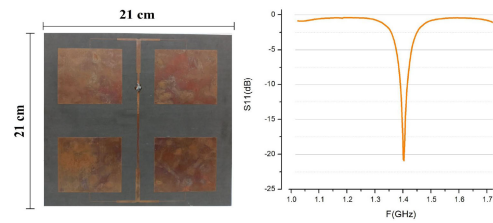

Fig. 4.   *L*-band antenna array (left) and measured input reflection coefficient (right).

clock frequency of 1 GHz, allowing for the UAV to scan the area faster or for improved radiometric resolution (ΔT) with a longer integration time. The 12-bit ADC samples at 1 MS/s, buffer 1 is a dynamic array with a size of $N = 128$, and buffer 2 stores and arranges the data retrieved from the sensors in HDF-EOS NASA format.

One aspect to be aware of when partitioning functionality from software into hardware is the implied overhead of communicating between the two parts of the system. The time taken to transfer data and instructions between software and hardware constitutes an additional latency that offsets the processing speed-up; if the overhead is too large, the benefit of hardware acceleration is lost [12]. In the ZYNQ architecture the communication overhead is low due to the tight coupling between the PS and PL components of the device through high-speed standard AXI interfaces [12].

IV. RF FRONT-END CHARACTERIZATION

The microwave emissions from the scanned surface area are captured by the antenna, and amplified and filtered by the front end. The following equation describes the power at the input of the detector:

$$P = K(T_A + T'_{\mathrm{REC}})BG \qquad (1)$$

where K is Boltzman's constant, T_A is the antenna temperature, T'_{REC} is the receiver noise temperature with transmission line losses, B is the bandwidth, and G is the total gain along the signal path.

A. Antenna Design and L-Band Front-End

The antenna was designed using microstrip technology; it is a 2×2 square array, with dimensions of 21 cm $\times$ 21 cm, with a bandwidth of 22 MHz. The radiometer bandwidth is limited to the 22 MHz of the antenna, since it is the component with the smaller bandwidth. This radiometer was designed to work in the 1400–1427 MHz protected band, and the antenna bandwidth supports the reduction of external noise and interference outside the operating band [13]. This design is somewhat smaller and lighter than the one used in [9]. Fig. 4 shows the antenna prototype and the input reflection coefficient response.

Table I gives the antenna specifications, and the radiation pattern is shown in Fig. 5. Simulations were performed in ANSYS HFSS. Note that the antenna has a gain of 12.5 dB, and a beamwidth of 52°, with no sidelobes.
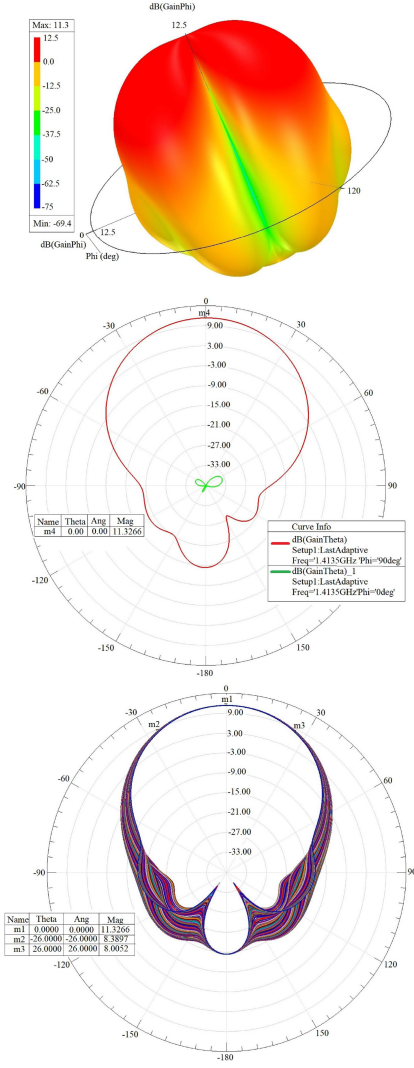
Fig. 5. *L*-band antenna radiations patterns simulations. Three-dimensional pattern (top), *E*-plane (red) and *H*-plane (green) patterns at 1.419 GHz (center). *E*-plane pattern frequency sweep from 1 to 2 GHz (bottom).

The *L*-band front-end comprises a high gain chain of low noise amplifiers ($G = 92$ dB) and band pass filters to attenuate out-of-band frequencies. The front-end components are LNA1 and LNA2: TAMP-1521GLN; BPF1 and BFP2: CBP-1400E; LNA3 and LNA4: ZX60-P33ULN+ (all from MiniCircuits [14], a 5 dB coaxial attenuator, and the ADL5511 detector from analog devices [15]. The total noise figure of the system (NFsys) was theoretically calculated to be 0.6 dB using the component datasheets and (2) and (3). This was verified experimentally with the Agilent E4404B spectrum analyzer in noise figure mode, at room temperature. The ADL5511 evaluation board was chosen to acquire the envelope of the output signal and to measure the RMS voltage. This device works from dc to 6 GHz, with minimum and maximum input power levels of −30 and 17 dBm, respectively

$$F\mathrm{sys} = F1 + \frac{(F2-1)}{G1} + \frac{(F3-1)}{G1*G2} + \frac{(F4-1)}{G1*G2*G3}$$

$$+ \frac{(F5-1)}{G1*G2*G3*G4} + \frac{(F6-1)}{G1*G2*G3*G4*G5}$$

$$+ \frac{(F7-1)}{G1*G2*G3*G4*G5*G6} \tag{2}$$

$$NFsys = 10 * \mathrm{Log}(F\mathrm{sys}). \tag{3}$$

B. Radiometer Resolution

To calculate the radiometer resolution, the noise temperature due the electronics components of the receiver, T_{REC}, was calculated using (4). $F\mathrm{sys} = 1.14$, and $T_0 = 290$ K, therefore $T_{\mathrm{REC}} = 40.6$ K. The receiver noise temperature referred to the antenna terminals T'_{REC}, including the transmission line losses L was calculated from (5), and found to be $T'_{\mathrm{REC}} = 232.34$ K, with $L = 2$ dB, and T_0 and $Tp = 290$ K.

Finally, the ideal resolution, ΔT, was calculated with (6), with $T_A = 300$ K. For an integration time, $\tau = 4$ ms, $\Delta T = 1.7$ K; and $\Delta T = 1$ K for $\tau = 12$ ms. The processing and low-pass filtering was implemented digitally and τ can be changed dynamically in runtime to maintain the resolution below 2 K

$$T_{\mathrm{REC}} = (F\mathrm{sys} - 1)\, T_0 \tag{4}$$

$$T'_{\mathrm{REC}} = (L-1)\, T_p + L * T_{\mathrm{REC}} \tag{5}$$

$$\Delta T = \Delta T\mathrm{sys} = \frac{T\mathrm{sys}}{\sqrt{B\tau}} = \frac{T_A + T'_{REC}}{\sqrt{B\tau}}. \tag{6}$$

The gain variation ($\Delta G/G = 0.002$) was obtained using an input signal of −100 dBm at 1.419 GHz, with the front-end physical temperature Tp changing from 290 to 313 K, and measuring the gain variations of the output signal in the Agilent E4404B spectrum analyzer, which resulted in $\Delta G = 0.21$ dB. The front-end total gain is $G = 92$ dB at $Tp = 290$ K, therefore, the experimental resolution at room temperature (290 K) was calculated using (7) ($\Delta T = 2$ K, when $\tau = 4$ ms, and $\Delta T = 1.48$ K, when $\tau = 12$ ms)

$$\Delta T = T\mathrm{sys}\left[\frac{1}{B\tau} + \left(\frac{\Delta G}{G}\right)^2\right]^{1/2}. \tag{7}$$

C. Calibration Process

The approach shown by Ulaby *et al.* [16] was used to calibrate the radiometer. Two known noise sources T_{cal1} (Agilent N4000A ENR = 6 dB) and T_{cal2} (Agilent 346B ENR = 14.6 dB), along with a third reference, the antenna pointing at zenith direction toward the sky at night [17] (10 K) without the presence of the moon, where used for this purpose. The noise sources were used as input to the receiver instead of the antenna, and the RMS voltage at the output of the detector AD5511 was measured using an oscilloscope for the three references. The output is shown in Fig. 6, and (8) describes the linear regression from the experimental points

$$V\mathrm{outRMS} = 6.71x10^{-5} * T\mathrm{cal} + 0.289. \tag{8}$$

The radiometer was characterized and calibrated at different physical temperatures ranging from 287.15 to 308.15 K
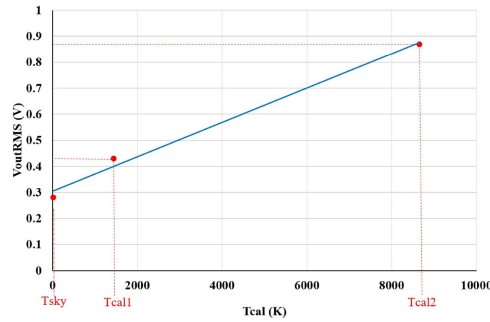
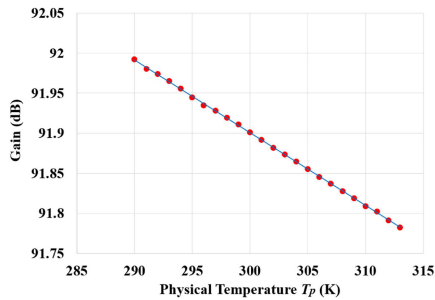Fig. 6.   Calibration curve for radiometer.

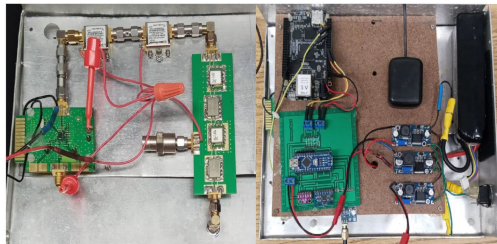Fig. 7.   Front-end gain versus physical temperature.

Fig. 8.   Front-end receiver (left) and the radiometer circuit (right).

(see Fig. 7). The implemented algorithm constantly measures the physical temperature inside the radiometer with the GY-BME280 sensor, to correct for the actual gain. Fig. 8 shows the RF receiver and the radiometer circuit.

V. PROCESSING ALGORITHM AND OPTIMIZATIONS

A. High Level Optimizations

To reduce the digital receiver power consumption, several high-level optimizations were applied to the main program in C++, running on the ARM microprocessor and the ZYNQ7010. Loop-oriented, memory management level, and function level optimizations were tested to quantify their effects on execution speed and power consumption.

The loop-oriented optimizations tested include loop unrolling (LU) and loop fission (LF) [18]. LU speeds up the code by reducing the number of long jumps at the end of each loop, and, therefore, reducing power [19]. LF splits a big loop into multiple loops using shorts jumps instead long jumps [18]. At the memory management level, we tested static memory allocation (SMA) and dynamic memory allocation (DMA). DMA, as opposed to
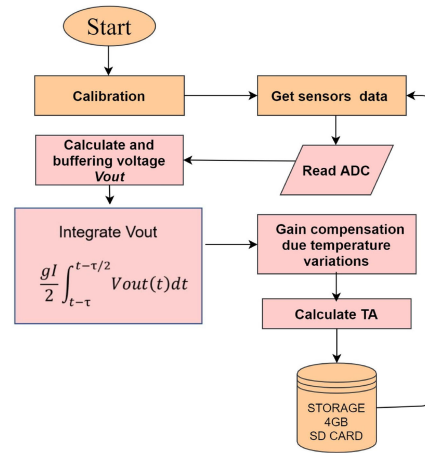

Fig. 9.   Flowchart of the proposed algorithm with ARM A8 microprocessor and ZYNQ 7010.

SMA, requests needed space in memory during the run time; in SMA the memory space is assigned during the compilation process [20]. At function level we tested Function Inlining (FI), FI optimization replaces a function with the body of the called function [21], but excess inlining will hurt speed due to size of the compiled code. Finally, the processors low power modes were explored, by forcing the processing system (ARM or ZYNQ) to go to "*sleep*" state during inactive time intervals.

The proposed processing algorithm was split into several tasks, as shown in Fig. 9. The first step is the calibration, described in Section IV. Then, the values of the auxiliary sensors, such as altimeter, GPS, gyroscope, magnetometer, and temperature, are retrieved from the sensors board. Subsequently, the data from the antenna (observed scene footprint) is buffered from the ADC in chunks of $N = 128$ integer values and fetched into a dynamic array. This raw data are processed using numerical integration (trapezoidal rule) with integration gain of $g_I = 1$ and variable integration time τ. Then, the received noise power is compensated according to the physical temperature variations ($\Delta G/G = 0.002$) to calculate the T_A values. Finally, the T_A values are stored into the SD card along with the sensors data using HDF-EOS NASA format. The Beaglebone Black ARM 8 microprocessor performs all the system tasks; for the ZYNQ 7010 the tasks are divided into the microprocessor side and the FPGA side. The algorithm was implemented in C++ programming language.

B. Intermittent Scanning Footprint (ISF)

To further increase power savings, we implemented an efficient scanning method based on the low power modes of the processing system (Beaglebone Black or ZYNQ 7010). Fig. 10 shows the concept; the UAV flies at a constant speed and height, thus, after scanning a determined footprint and processing the corresponding data, the processing system is forced into "*sleep*" mode until the limit of the next footprint is reached, where the system is then reawakened. This inactive time interval, or processing unit sleep time (PUST)*,* is calculated based on the execution time, according to the results of Section VI. We used a
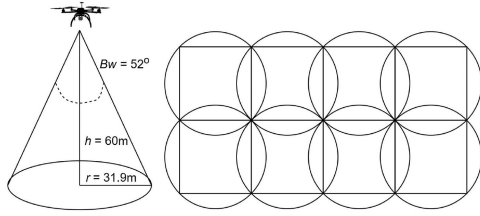
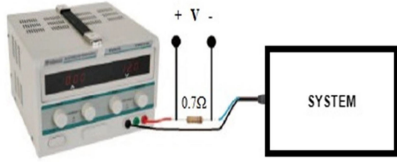Fig. 10.   Proposed ISF scanning method.

Fig. 11.   Instrumentation setup for current measurements.

drone with a gimbal platform stabilizer that holds the radiometer in horizontal position so the scanning was done at nadir angle.

The PUST is determined with (9) with the drone speed Vd, the antenna beamwidth Bw, the heigh h and the algorithm execution time t_{exec}

$$\text{PUST} = 2 * \tan(Bw/2) * h/Vd - t_{exec}. \qquad (9)$$

For example, $Vd = 10$ m/s, $Bw = 52°$, $h = 60$ m, and $t_{exec} = 30$ ms produce a PUST of 5.8 s.

C. Fixed Point Arithmetic

Fixed point arithmetic is an alternative to efficiently process data in terms of performance and power consumption, while maintaining good precision. A fixed-point number representation is a real data type that has a fixed number of digits before and after the radix point. This data representation is simpler than the more computationally demanding floating-point, because the operations are reduced to simple integer operations, such as addition and bit shifting [22]. In the experiments, the fixed-point format $Q(16,16)$, with a precision of 1/65536 was used. Section VI shows the differences in terms of power and execution time in comparison with floating-point.

D. Instrumentation for Power Consumption Measurements

The power consumption was measured using the setup shown in Fig. 11. A resistor of 0.7 Ω is placed in series with the power supply at 5.0 V and the high precision multimeter FLUKE RMS187 is used to measure the voltage. The current is calculated using Ohm's law.

VI. Results and Discussion

A. Performance and Power Consumption

The experiments of power consumption and system performance were done at different clock frequencies, 1 GHz, 600 MHz and 300 MHz, and comparing the implementation of the algorithm with floating-point versus fixed-point. Figs. 12–14 show the power consumption of the Beaglebone Black board
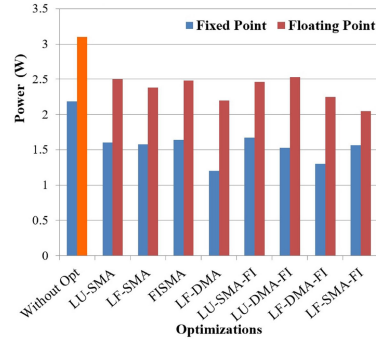

Fig. 12.   Beaglebone black power consumption at 1 GHz, $\tau = 7$ ms, and $N = 128$.
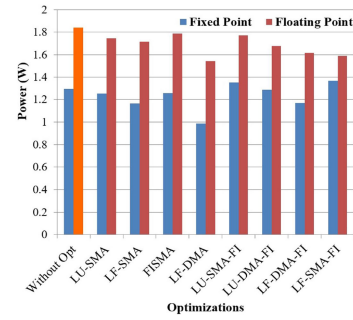

Fig. 13.   Beaglebone black power consumption at 600 MHz, $\tau = 7$ ms, and $N = 128$.
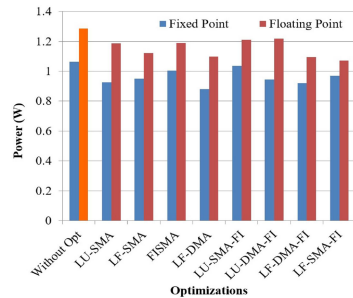

Fig. 14.   Beaglebone black power consumption at 300 MHz, $\tau = 7$ ms, and $N = 128$.

running the algorithm to process radiometric data versus optimizations. The optimizations were applied to the running source code written in C++. The results showed that floating-point processing LF-DMA, LF-DMA-FI, and LF-SMA-FI optimizations were significant in reducing power consumption. This is because DMA is more efficient at memory management and LF reduces the power demanding long jumps at assembly level. An interesting observation is that the fixed-point $Q(16,16)$ implementation reduced the power consumption significantly in all cases. In addition, these results confirmed that power consumption is inversely proportional to the microprocessor clock frequency.

The behavior of the execution time in the Beaglebone Black running the floating-point version of the algorithm is shown in Figs. 15–17. Execution time was improved significantly with FI-SMA and LU-SMA-FI optimizations; however, for the
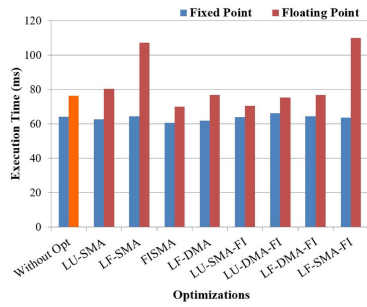
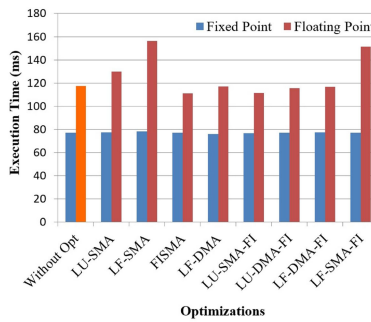Fig. 15. Beaglebone black execution time at 1 GHz clock, $\tau = 7$ ms, and $N = 128$.

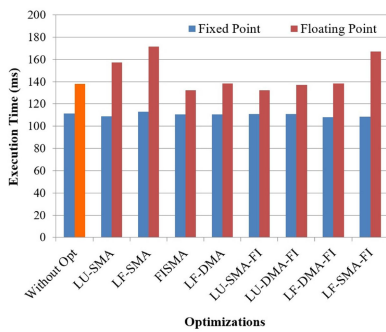Fig. 16. Beaglebone black execution time at 600 MHz clock, $\tau = 7$ ms, and $N = 128$.

Fig. 17. Beaglebone black execution time at 300 MHz clock, $\tau = 7$ ms, and $N = 128$.
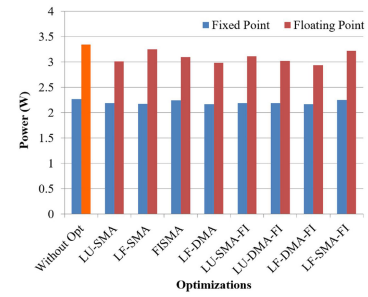

Fig. 18. ZYNQ 7010 power consumption at 1 GHz, $\tau = 7$ ms, and $N = 128$.
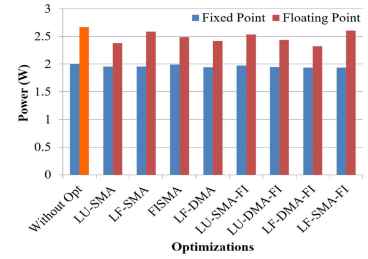

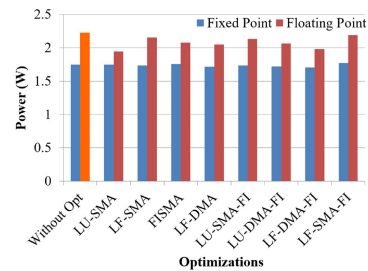Fig. 19. ZYNQ 7010 power consumption at 600 MHz, $\tau = 7$ ms, and $N = 128$.

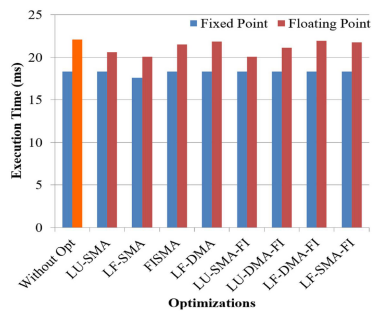Fig. 20. ZYNQ 7010 power consumption at 300 MHz, $\tau = 7$ ms, and $N = 128$.

Fig. 21. ZYNQ 7010 Execution time at 1 GHz, $\tau = 7$ ms, and $N = 128$.

LU-SMA, LF-DMA, LU-DMA-FI, and LF-DMA-FI optimizations, the difference in execution time was not significant in comparison with the algorithm without optimizations. In the cases of LF-SMA and LF-SMA-FI the execution time was affected adversely. This is because SMA saves the variables inside memory during the compiling process; therefore, when the program starts running, the CPU can access the variables easily and quickly, saving time [20]. In the case of LF the "for" loops are split, improving the power consumption, but the size of the code is increased, and the CPU spends more time reading the instructions from memory [18].

Figs. 18–20 show the results of power consumption for the ZYNQ 7010. The impact of the optimizations in the power reduction was not very significant, i.e., less than 7% with the floating-point version of the algorithm. However, the fixed-point processing reduced the power consumption significantly in the range of 23% and 30%. In addition, the optimizations had no effect, compared to the "without optimizations" value. In the case of execution time, it was reduced less than 7% in the best scenario of the floating-point cases, in contrast with the fixed-point processing the execution time was reduced between 22% and 25%, but there was no significant difference between optimizations (see Figs. 21–23).
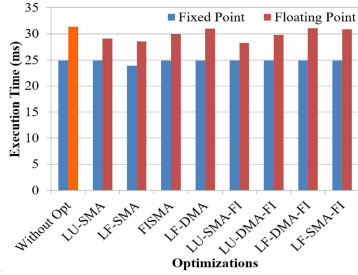
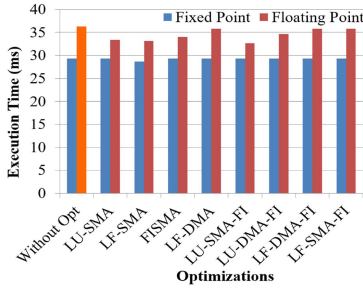Fig. 22. ZYNQ 7010 Execution time at 600 MHZ, $\tau = 7$ ms, and $N = 128$.

Fig. 23. ZYNQ 7010 execution time ZYNQ at 300 MHz, $\tau = 7$ ms, and $N = 128$.

VII. HEURISTIC METHODOLOGY TO SAVE POWER AND INCREASE THE PERFORMANCE

Based on the aforementioned results, we designed a heuristic methodology to reduce power consumption and increase the performance considering the processing in the ARM A8 and ZYNQ 7010 architectures. Fig. 24 shows the proposed methodology. The program was developed using C++ as programming language under Linux Debian V8 since it is lightweight and provides high performance. One of the main aspects to consider is that the data from the sensors board and radiometer was merged and formatted according to the EOS remote sensing standard from NASA. The characterization of the algorithm allows us to know how demanding reading and writing in memory is, because the accesses to memory are the most power expensive instructions and the largest cause of latency [20]. Consistent with this, it is necessary to minimize the accesses to the secondary memory SD card; the best approach is writing the SD card in small packages of data, for example a size of $N = 128$ characters, and using an ADC sampling buffer of the same size. This approach is more efficient than writing one value at a time. The next step in the heuristic methodology is to implement the ISF method, applying the low power mode (*sleep*) of the ARM A8 and ZYNQ 7010 architecture saving power and memory resources accesses. The PUST is determined with (9).

The next step is applying the high-level optimizations DMA, FI, and LF to the main program running on the ARM A8, whereas for the ZYNQ 7010 the approach is based in the distribution of the load between the FPGA and the ARM microprocessor side. According to Fig. 24, the FPGA executes the most demanding computational operations and calculations, and the microprocessor side executes the sensors data acquisition and formatting, sampling, buffering, and control. The sampling buffer needs to
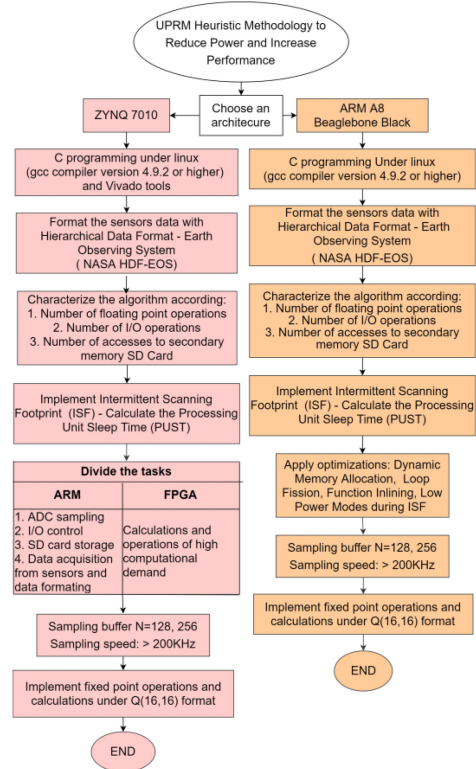

Fig. 24. Heuristic methodology to reduce power consumption and increase performance in radiometric data processing.

have sizes of $N = 128$ or 256 to simplify binary operations. Moreover, the buffer cannot be too small because it affects the continuity of the footprint sampling and will increase the memory accesses, nor can it be too large because it will take longer times writing in memory, adversely impacting performance. Finally, the fixed-point representation $Q(16,16)$ should be implemented to replace the complex operations with high computational demand with simpler operations using the integer representation of the floating point numbers [6].

VIII. SALINITY MEASUREMENTS AND VALIDATION

Preliminary results of our work were presented in [10], where two controlled salinity experiment were performed. In the first one, different amounts of sea salt were poured and mixed with tap water in a tank of approximately 60 cm diameter. In the second one, the test was repeated with sea water at Magüeyes Island, and tap water was added to reduce the salinity. The radiometer was placed just on top, 30 cm from the water level, to allow the footprint area of the antenna cover the water. In this article, several tests to measure brightness temperature and salinity were done at Magueyes Island, off the coast of Lajas, Puerto Rico, and the coast of Añasco. The commercial portable salinometer YSI-599501-02 was used to measure salinity *in situ* and validate our results (see Fig. 25). The instrument was carried on a kayak trying to follow the same path as the drone going from the shore to about 300 m toward the open ocean.

Fig. 25.   EXO-YSI 599501-02 instrument.

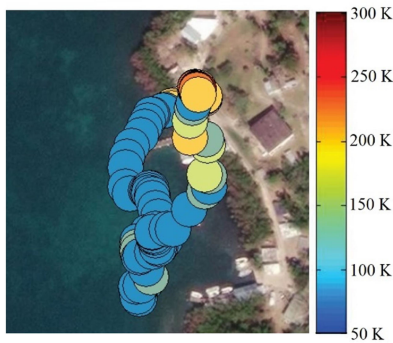Fig. 26.   Drone overflying the Magueyes island coast.

Fig. 27.   Brightness temperature map over Magueyes Island.
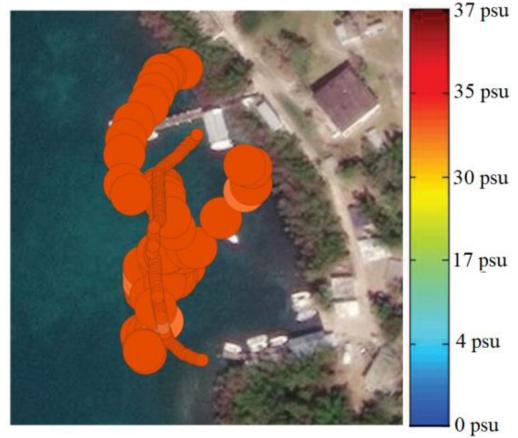

Fig. 28.   Salinity map of radiometer (large circles) versus YSI-599501 instrument (small circles) over Magueyes Island. The radiometer circle sizes represent the antenna footprint.
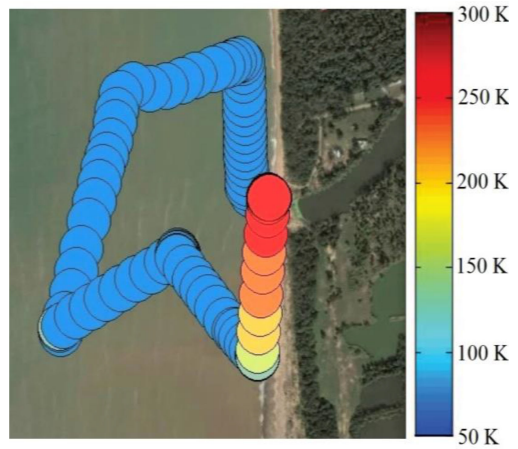

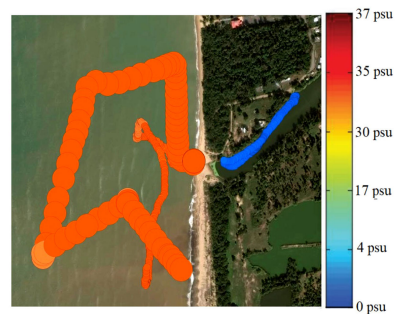Fig. 29.   Brightness temperature map over the coast of Añasco, Puerto Rico.

Fig. 30.   Salinity map of radiometer (large circles) versus YSI-599501 instrument (small circles) over the coast of Añasco, Puerto Rico. The radiometer circle sizes represent the antenna footprint.

A. Campaign on Magueyes Island

The Magueyes island location is in GPS coordinates 17.969982, -67.046281. Fig. 26 shows the drone flying over the area with the radiometer in horizontal position. The drone maximum speed was 10 m/s.

The salinity model proposed by Klein *et al.* [23] was used to convert the brightness temperature into PSU salinity units. The values of salinity measured by the radiometer were between 34.07 to 36.5 PSU with brightness temperature ranging from 91.2 to 92.5 K, as shown in Figs. 27 and 28. The YSI-599501 measured between 33.64 to 33.71 PSU with a physical water temperature of 27.69 °C, therefore the error was between 1% to 8.1%. Some sources of error were introduced by the surrounding environment and the smooth movement of the water due the wind.

B. Campaign on the Añasco River Mouth

Two flights were performed over the coast of Añasco at coordinates 18.272039, -67.189567 at an approximate height of 40 m, in the vicinity of the Añasco River mouth. The first flight covered the sea and the shore, as shown in Fig. 29, the second goes into the river (see Fig. 31). The measured brightness temperature was between 90 K y 91.1 K and the salinity values calculated by the radiometer were from 34.9 PSU to 37.42 PSU. The YSI-599501 salinity readings were from 34.58 to 34.62 PSU, with a physical water temperature of 27.70 °C, therefore the resultant error was between 1% and 8.3%. This can be seen in
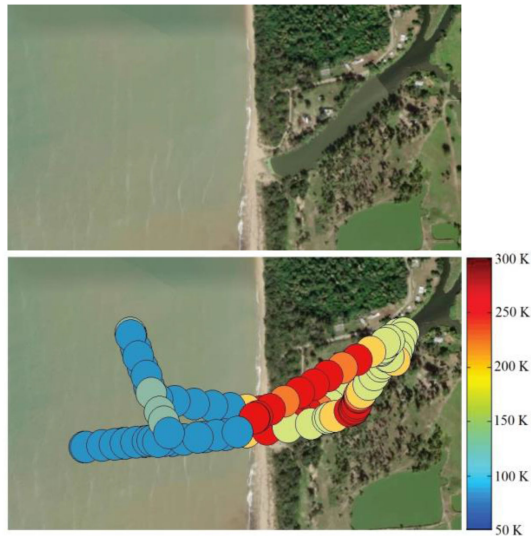
Fig. 31. Measurement area (top) and brightness temperature map (bottom) for the experiment crossing between the sea to the river. Note that the river mouth is closed off by sediments.
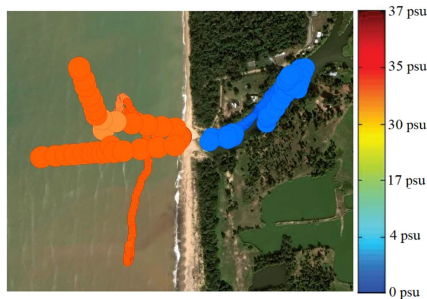

Fig. 32. Salinity map of radiometer (large circles) vesus YSI-599501 instrument (small circles) for the experiment crossing between the sea to the river. The radiometer circle sizes represent the antenna footprint.

Figs. 30 and 32. These results demonstrated that ocean salinity measurements were very similar around the area under study. It is important to highlight that the brightness temperature in the sea water was much less in comparison with the sand, vegetation, and the fresh water in the river, since the saltwater is more electrically conductive and reduces the energy emitted in the L-band microwave frequency of 1.4 GHz [24].

In addition, the river did not flow freely into the sea, as shown in Fig. 31, consequently we can observe an abrupt change in brightness temperature between the river and the sea. The YSI-599501 measured a salinity of 0.69 to 0.84 PSU in the river; similarly, the radiometric brightness temperature measured over the river increased to approximately to 160 K $\pm$ 2K and the salinity calculations were from 0.7 to 0.93 PSU (1.4% to 10% error), as seen in Fig. 32.

IX. CONCLUSION

This article presented the design and construction of a low SWaP receiver for a small UAV-mounted, L-band radiometer. Two architectures, the ARM A8 and ZYNQ 7010 were studied to process data more efficiently and reduce power consumption.

The results demonstrate that the proposed Heuristic Methodology and the ISF method (low power modes) reduced the power of the ARM to 1.5 W at 1 GHz clock speed and the execution time to 65 ms. The ZYNQ 7010 processed the data faster, at approximately 19 ms and 2.3 W of power consumption. The optimizations did not have significant impact in power saving on the ZYNQ 7010, the approach for power reductions in this kind of hybrid architecture was the division of the workload between the FPGA and the ARM A9 microprocessor, however the DMA, LF, FI optimizations worked very well for ARM A8 microprocessor. In addition, the fixed-point representation Q (16,16) improved the power and the execution time in both architectures. It is important to highlight that, according to the experiments, the total energy savings on the radiometer during a 20-min flight was 48%. This article showed that both architectures can be used to process radiometric data in remote sensing applications such as salinity measurements with a resolution ($\Delta T < 2$ K) and integration times higher than 4 ms ($\tau > 4$ ms). The final size of the built radiometer is 30 cm $\times$ 30 cm, and weights 1.35 kg (3 lb). Future work includes building a Dicke-type version of the radiometer to minimize the gain variations with respect to the physical temperature of the RF receiver. Finally, another contribution of this article is that the proposed heuristic methodology can be used in other embedded systems applications based on the ARM and ZYNQ 7010 architectures.

REFERENCES

[1] Y. Sawada, H. Tsutsui, T. Koike, M. Rasmy, R. Seto, and H. Fujii, "A field verification of an algorithm for retrieving vegetation water content from," *IEEE Trans. Geosci. Remote Sens.*, vol. 54, no. 4, pp. 2082–2095, Apr. 2016.

[2] D. Liu, C. Lv, K. Liu, Y. Xie, and J. Miao, "Retrieval analysis of atmospheric water vapor for K-band ground-based hyperspectral microwave radiometer," *IEEE Geosci. Remote Sens. Lett.*, vol. 11, no. 10, pp. 1835–1839, Oct. 2014, doi: 10.1109/LGRS.2014.2311833.

[3] E. Dai, A. Gasiewski, M. Stachura, and J. Elston, "L-band soil moisture mapping using a SUAS for validation and calibration of SMAP," in *Proc. IEEE Int. Geosci. Remote Sens. Symp.*, 2016, pp. 3134–3136, doi: 10.1109/IGARSS.2016.7729810.

[4] R. Acevo-Herrera, A. Aguasca, X. Bosch-Lluis, and A. Camps, "On the use of compact L-band Dicke radiometer (ARIEL) and UAV for soil moisture and salinity map retrieval: 2008/2009 field experiments," *Int. Geosci. Remote Sens. Symp.*, vol. 4, pp. 729–732, 2009, doi: 10.1109/IGARSS.2009.5417480.

[5] A. D. Marinan *et al.*, "Assessment of radiometer calibration with GPS radio occultation for the MiRaTA CubeSat mission," *IEEE J. Sel. Topics Appl. Earth Observ. Remote Sens.*, vol. 9, no. 12, pp. 5703–5714, Dec. 2016, doi: 10.1109/JSTARS.2016.2598798.

[6] D. Mera and R. Solis, "Power and performance analysis for a small L-band total power radiometer," in *Proc. IEEE MTT-S Latin Amer. Microw. Conf.*, 2018, pp. 1–4. doi: 10.1109/LAMC.2018.8699048.

[7] M. Asif, X. Guo, J. Zhang, and J. Miao, "An FPGA based 1.6 GHz cross-correlator for synthetic aperture interferometric radiometer," in *Proc. Prog. Electromagn. Res. Symp.Fall*, 2017, pp. 1078–1085, doi: 10.1109/PIERS-FALL.2017.8293294.

[8] K. Cahoy *et al.*, "Development of the microwave radiometer technology acceleration (MiRaTA) CubeSat for all-weather atmospheric sounding," in *Proc. Int. Geosci. Remote Sens. Symp.*, 2015, pp. 5304–5307, doi: 10.1109/IGARSS.2015.7327032.

[9] D. Mera and R. Solis, "Low power and miniaturized back-end processing system for an L- band Radiometer based on ARM embedded microprocessor," in *Proc. IEEE Radio Wireless Symp.,* 2019, pp. 1–4, doi: 10.1109/RWS.2019.8714392.

[10] D. Mera, R. Rodriguez, and S. Lorenzo, "Impact of high level optimizations on power consumption and performance of a small L-band total power radiometer," in *Proc. IEEE Radio Wireless Symp.*, 2020, pp. 83–86.

[11] D. Molloy, *Exploring Beaglebone*. Indianapolis, IN, USA: Wiley, 2015.

[12] R. Crockett, L. Elliot, R. Enderwithz, and M. Stewart, *The Zynq Book*, 1st ed. Glasgow, U.K.: Media, Strathclyde Academic, 2014.

[13] Y. Kerr *et al.*, "New radiometers: SMOS a dual pol L-band 2D aperture synthesis radiometer," in *Proc. IEEE Aerosp. Conf. Proc.,* 2000, pp. 119–128, doi: 10.1109/AERO.2000.878481.

[14] H. Ted, "Minicircuits.com," 2020. [Online]. Available: https://www.minicircuits.com/

[15] V. Roche, "Analog devices," 2021. [Online]. Available: https://www.analog.com

[16] F. T. Ulaby *et al.*, *Microwave Radar and Radiometric Remote Sensing*. Ann Arbor, MI, USA: Univ. Michigan Press, 2014, pp. 263–319.

[17] M. Schwank *et al.*, "ELBARA II, an L-band radiometer system for soil moisture research," *Sensors,* vol. 10, no. 1, pp. 584–612, Jan. 2010, doi: 10.3390/s100100584.

[18] S. Sushko and A. Chemeris, "The dependence of microprocessor system energy consumption on software optimization," in *Proc. IEEE 37th Int. Conf. Electron. Nanotechnol.*, 2017, pp. 451–454.

[19] G. Velkoski, M. Gusev, and S. Ristov, "The performance impact analysis of loop unrolling," in *Proc. IEEE 37th Int. Conv. Inf. Commun. Technol., Electron. Microelectron.*, 2014, pp. 26–30.

[20] I. Deligiannis and G. Kornaros, "Adaptive memory management scheme for MMU-less embedded systems," in *Proc. 11th IEEE Int. Symp. Ind. Embedded Syst.*, 2016, pp. 1–8, doi: 10.1109/SIES.2016.7509439.

[21] A. Gordon-Ross, A. Munir, and R. Sanjay, *Modeling and Optimization of Parallel and Distribuited Embedded Systems*. New York, NY, USA: Wiley, 2016, pp. 141–342.

[22] W. Padgett and D. Anderson, *Fixed-Point Signal Processing*. San Rafael, CA, USA: Morgan & Claypool, 2009, pp. 31–52.

[23] L. Klein and C. Swift, "An improved model for the dielectric constant of sea water at microwave frequencies," *IEEE J. Ocean. Eng.*, vol. 2, no. 1, pp. 104–111, Jan. 1977.

[24] C. Gabarró, M. Vall-Llissera, J. Font, and A. Camps, "Determination of sea surface salinity and wind speed by L-band microwave radiometry from a fixed platform," *Int. J. Remote Sens.*, vol. 25, no. 1, pp. 111–128, 2010, doi: 10.1080/0143116031000115175.

Daniel Ernesto Mera (Member, IEEE) was born in Sandoná, Nariño, Colombia. He received the Bachelor's degree in electronics engineering from the National University of Colombia, Bogotá, Colombia, in 2007, and the M.S. degree in computer engineering with specialization in embedded systems in 2010 from the University of Puerto Rico at Mayagüez, Mayagüez, PR, USA, where he is currently working toward the Ph.D. degree in electrical engineering.

His research interests include low power embedded systems, microwave remote sensing, and rapid system prototyping.

Rafael A. Rodríguez Solís (Senior Member, IEEE) was born in Santurce, PR, USA. He received the B.S.E.E. and the B.S.CpE. degrees from the University of Puerto Rico at Mayagüez, Mayagüez, PR, USA, in 1990, the M.S. degree in electrical engineering from the University of Florida, Gainesville, FL, USA, in 1993, and the Ph.D. degree in electrical engineering from Pennsylvania State University, State College, PA , USA, in 1997.

He is currently a Professor of electrical and computer engineering with the University of Puerto Rico, Mayagüez, PR, USA, where he is currently the Director of the UPRM Microwave Antennas and Remote Sensing Systems Laboratory, and as the UPRM PI for the NOAA EPP Collaborative Science Center for Earth System Sciences and Remote Sensing Technologies.

Dr. Rodríguez Solís was the recipient of an NSF CAREER Award in 2001, and was a NASA Glenn Research Center Summer Faculty Fellow in 2012. He was a member of the IEEE Antennas and Propagation Society Education Commitee and was Co-Chair of the IEEE International Symposium on Antennas and Propagation in 2016.

Lorenzo Reyes (Member, IEEE) was born in Santurce, Puerto Rico. He is currently working toward the B.S. degree in electrical engineering with the University of Puerto Rico at Mayagüez, Mayagüez, PR, USA.

As a freshman, he was a part of the IEEE Student Chapter Scholar Program and was a part of the board of directors as the treasurer. In 2018, he was a Summer Bridge Student Fellow for the NOAA-CREST Summer Bridge Program and he is currently a NOAA EPP Earth System Sciences and Remote Sensing Scholar.

Roy Armstrong received the Bachelor's degree in biology from Boston University, Boston, MA, USA, in 1976, and the Master's and Doctorate degrees in marine sciences from the University of Puerto Rico at Mayagüez (UPRM), Mayagüez, PR, USA, in 1982, and 1990, respectively.

As a graduate student in the Department of Marine Sciences he pioneered the use of remote sensing technology for studies of the marine environment in Puerto Rico. After finishing the Ph.D. in 1990, he spent four years with NASA's Ames Research Center as a National Research Council Post-doctoral Fellow and a Research Associate working with hyperspectral remote sensing. Upon his return to Puerto Rico, with funding from NASA and NOAA, he established the Bi-optical Oceanography laboratory at UPRM. His research interests include highly interdisciplinary, being mainly concerned with water optics, airborne and satellite remote sensing, coral reef ecology and bio-optics, and the effects of Sahara dust aerosols in the eastern Caribbean.

William J. Hernández was born in Mayagüez, Puerto Rico. He received the Doctoral degree in marine sciences from the University of Puerto Rico, Mayagüez, PR, USA, in 2016, with his research specialized in bio-optical oceanography and remote sensing.

He also continued his post doctoral studies as a fellow of the NOAA Center for Earth Systems Science and remote Sensing Technologies, City College, City University of New York, New York, NY, USA. He is currently an Adjunct Professor of electrical and computer engineering, and a Researcher for the Research and Development Center, University of Puerto Rico, Mayagüez, PR, USA.

Alba L. Guzmán Morales was born in Arecibo, Puerto Rico. She received the B.S. degree in biology in 2019 from the University of Puerto Rico, Mayagüez (UPRM), Mayagüez, PR, USA, where he is currently working toward the M.S. degree in biological oceanography.

She is a member of the Bio-optical Oceanography Laboratory, UPRM and a NOAA Cooperative Science Center in Atmospheric Sciences and Meteorology fellow.